Xiang, Hang, Rasul, Shahid, Hou, Bo , Portoles, Jose, Cumpson, Peter and Yu, Eileen H. 2020. Copper-indium binary catalyst on a gas diffusion electrode for high-performance CO2 electrochemical reduction with record CO production efficiency. ACS Applied Materials and Interfaces 12 (1) , pp. 601-608. 10.1021/acsami.9b16862

Publishers page: http://dx.doi.org/10.1021/acsami.9b16862

Copper-indium binary catalyst on gas diffusion electrode for high-performance CO_2 electrochemical reduction with record CO production efficiency

Hang Xiang[1], *Shahid Rasul*[1,2], *Bo Hou*[3], *Jose Portoles*[1], *Peter Cumpson*[1], *Eileen H. Yu*[1] *

[1] School of Engineering, Newcastle University, Newcastle Upon Tyne

[2] Faculty of Engineering and Environment, Northumbria University, Newcastle Upon Tyne

[3] Engineering Department, University of Cambridge, Cambridge

Corresponding Author

*(eileen.yu@ncl.ac.uk)

KEYWORDS

Cu-In binary catalysts, electrochemical CO_2 reduction, CO selectivity, electrochemical spontaneous precipitation, production rate, ultrathin layer, current density.

ABSTRACT

Cu-In metallic hybrid is a promising non-noble catalyst for selective electrochemical CO_2 reduction (eCO_2R) to CO, but the lack of direct assembly with gas diffusion electrode (GDE) limits the further development of eCO_2R to CO with both high Faradaic efficiency (FE) and high current density. In this study, an *in-situ* electrochemical spontaneous precipitation (ESP) method was applied for the first time to prepare GDE-combined Cu-In electrocatalysts. The optimum Cu-In catalyst consists of an nano-scale "core-shell" structure of polycrystalline Cu_xO covered by amorphous $In(OH)_3$ interface. Higher than 90% Faradaic efficiency of CO production has been achieved. With the synergy of a GDE flow-cell and 1 M KOH catholyte, a current density of ~200 mA cm^{-2} was reached at -1.17 V (RHE), which enabled a CO yield efficiency record of 3.05 mg min^{-1} (CO_2/15 ml min^{-1} with 2 cm^2 electrode). The ratios between CO and H_2 produced can be effectively modulated via fine-tuning ESP conditions demonstrating possibility of generating CO or syngas with tuneable ratios. The present study provides a simple approach for constructing novel catalytic interfaces with dual active centers for eCO_2R and other emerging electrochemical catalysis research.

1. INTRODUCTION

Electrochemical CO_2 reduction (eCO_2R) has attracted significant interests in CO_2 utilisation field in recent years, which is well-known to be a sustainable and cost-effective route among the CO_2 conversion pathways[1]. Only water and renewable electricity would be consumed as the inputs to convert CO_2 into value-added carbonaceous products on the cathodic side, meanwhile with pure O_2 evolution at the anodic side as the by-product. However, in aqueous electrolyte, CO_2 mass transfer is constrained by the low CO_2-solubility, and the competitive hydrogen evolution reaction (HER) consumes electrons simultaneously and reduces the current efficiency of eCO_2R. To achieve a high reaction rate of eCO_2R as well as an exclusive selectivity towards one particular carbonaceous product is the common goal of this research filed[2-4].

CO is a promising product from eCO_2R as its industrial value for the production of fuels and chemicals[5-6]. The electrocatalysts for CO_2 reduction to CO are mostly reported to be bulk or nanostructured noble metals or their oxides such as Au[7-8], Ag[9-10], Pd[11-12] species. Some metal-free carbon materials were also presented to perform high CO selectivity from eCO_2R, such as carbon nanotubes[13-14] and graphene quantum dots[15] with doping nitrogen to modify the active sites. Those catalytic materials all bring their own cost and sustainable issues. Aiming at the practical use, the combination of multiple non-noble metals in the form of homogeneous alloy or heterogeneous composite should be a cost-effective approach for the design of catalytic materials. Rasul et al.[16-17] showed that by alloying two non-noble metals Cu and In for catalysing eCO_2R in CO_2-saturated aqueous electrolyte, a Faradaic efficiency (FE) of 90% for CO production was achieved. However, the reaction rate is low with a current density lower than 10 mA cm^{-2} at moderate potentials (about -1 V vs RHE).

Our previous work[18-19] demonstrated the slow reaction rate was caused by the limitation of CO_2 mass transfer in a traditional two-chambers reactor with CO_2-saturated catholyte, and the low current density to a large extent was resulted from using dilute carbonate/bicarbonate catholyte. A combination between gas diffusion electrode (GDE) and strong alkaline catholyte can achieve a high current density of the reduction reaction, due to the developed CO_2 mass transfer of GDE and faster ion mobility of strong alkali [18, 20]. Herein, for the first time, we propose the GDE-combined Cu-In catalyst *in-situ* synthesized by a facile electrochemical spontaneous precipitation (ESP) method, to achieve high-performance eCO_2R to CO.

2. RESULTS AND DISCUSSION

2.1. Characterizations of Cu-In catalyst

The GDE-combined Cu-In catalyst was fabricated by ESP of In on Cu_2O coated gas diffusion layer (GDL), which is a Cu-rich combination with ultrathin $In(OH)_3$ layer on the surface, as suggested by the catalyst characterization in Figure 1. The XRD result (Figure 1a) of CuIn-ESP25min with the highest CO selectivity, which demonstrates the phase composition of the bulk electrode only shows Cu-related signals without a sign of indium. Compared to the precursor Cu_2O-GDL contained majorly Cu_2O and a small amount of CuO, polycrystalline Cu mainly constitutes the crystal structure of bulk CuIn-ESP25min, which indicates a reduction of Cu oxides during the ESP process. Even though indium species is undetectable by XRD, the XPS spectra in Figure 1b proves the existence of In on the surface, since the prominent photoelectronic peaks in In 3d spectrum are symmetrical at 445.1 eV and 452.5 eV assigned as In $3d_{5/2}$ and In $3d_{3/2}$ of $In(OH)_3$[21-22]. This hydroxide feature is also manifested in the XPS O1s spectrum, presented as M-OH peak which could be differentiated at ~532.5 eV[22-23]. The Cu2P spectrum also indicates the reduction of Cu species during ESP: the CuO peak area of CuIn-ESP25min at 933.9 eV in the $Cu2p_{3/2}$ region reduced compared to Cu_2O-GDL, so that Cu_2O or Cu (932.3 eV)[24-26] constituted the major Cu species on the surface of CuIn-ESP25min.

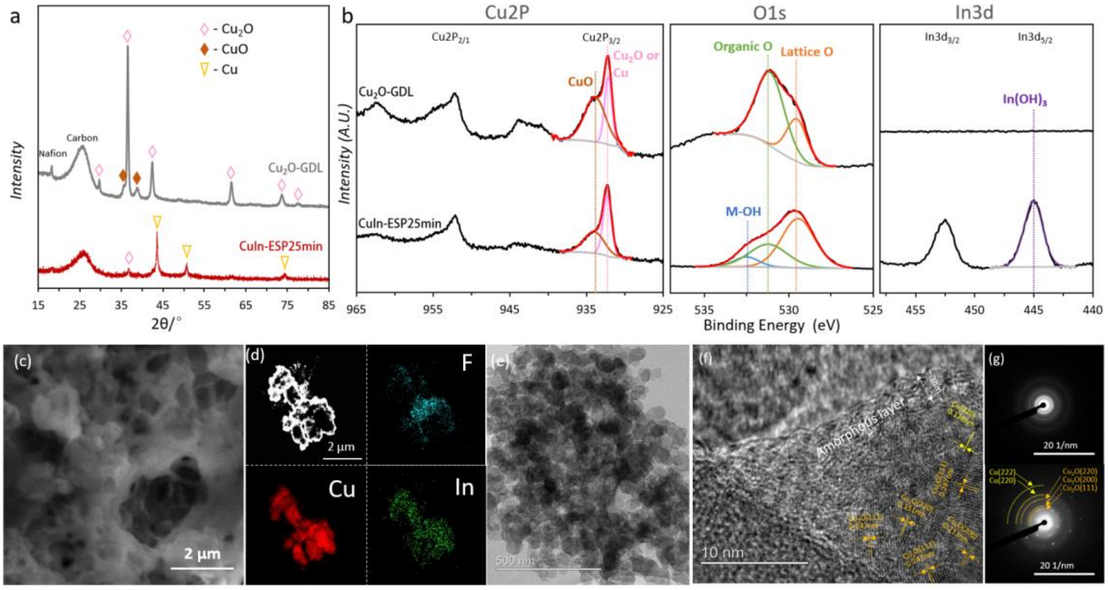

Figure 1. (a) XRD profiles and (b) High-resolution XPS spectrum of Cu 2p, O 1s, and In 3d of Cu_2O-GDL (top), CuIn-ESP25min (bottom). (c) SEM, (d) HAADF STEM image and element mapping, (e) TEM, (f) HRTEM, and (g) SAED of CuIn-ESP25min.

The morphology and microstructures of as-prepared Cu-In binary catalyst are systematically studied through electron microscopies analysis. As shown in Figure 1 c-g, the SEM image in Figure 1c shows the morphology of CuIn-ESP25min that irregular protrusions with about 0.5 - 2 μm dimension attaching on the reticular Nafion framework. The high-angle annular dark-field (HAADF) STEM image (Figure 1d) displays a typical protrusion in micro-scale with assembled microparticles bonded by Nafion. As shown in the STEM-EDX elemental mapping graphs, F mostly distributes in-between the micro-particles and Cu is the dominating composition which mostly distributed in the centre of microparticles while In covers more evenly on the whole particle. The TEM image in Figure 1e indicates the microparticle is an aggregate of nanoparticles with an average diameter of 50 nm. Atomic-scale high-resolution TEM (HRTEM) analysis (Figure 1f) presents typical diffraction contract images which demonstrate both crystalline and amorphous characteristics of the nanoparticles [27]. The bottom right region shows various crystal fringes with distances of 0.128, 0.151, 0.213, 0.247 nm represents Cu (220), Cu_2O (220), Cu_2O (200), and Cu_2O (111) respectively based on the ICDD database with PDF file No. 03-065-9743 and 01-078-2076. The featureless area shaped like a shell with 3~10 nm thickness tightly capping on the polycrystalline Cu phase, corresponds to the amorphous $In(OH)_3$ layer. The SAED images in Figure 1g show both amorphous and crystalline characteristics and the crystalline phase consists of polycrystalline Cu, and Cu_2O mixture (denoted as Cu_xO) agree with the lattice fringes in the HRTEM image[28-29]. The microscopy analysis indicates the amorphous/crystalline hybrid structure of CuIn-ESP25min: the nanolayer of amorphous $In(OH)_3$ capping on the polycrystalline Cu_xO.

2.2. The ESP method used for preparing Cu-In catalyst

This material was synthesised by a facile ESP method with 25 minutes. As presented in Figure 2a, the synthesis process starts from injecting the acidified In^{3+} solution (0.05

M $In_2(SO_4)_3$ and 0.4 M citric acid, pH = 2.5) into a container until immersing the two electrodes, a Cu_2O-binded GDL and a pure In foil, which are externally connected by a 2 Ω cable. One-hour ESP experimental phenomenon is also shown. The open-circuit voltage (OCV) between these two electrodes is initially 0.68 V as presented in Figure 2b. The current variation recorded within one-hour ESP is shown in Figure 2c; the charge over ESP time calculated by integrating the current-time curve is presented in Figure 2d.

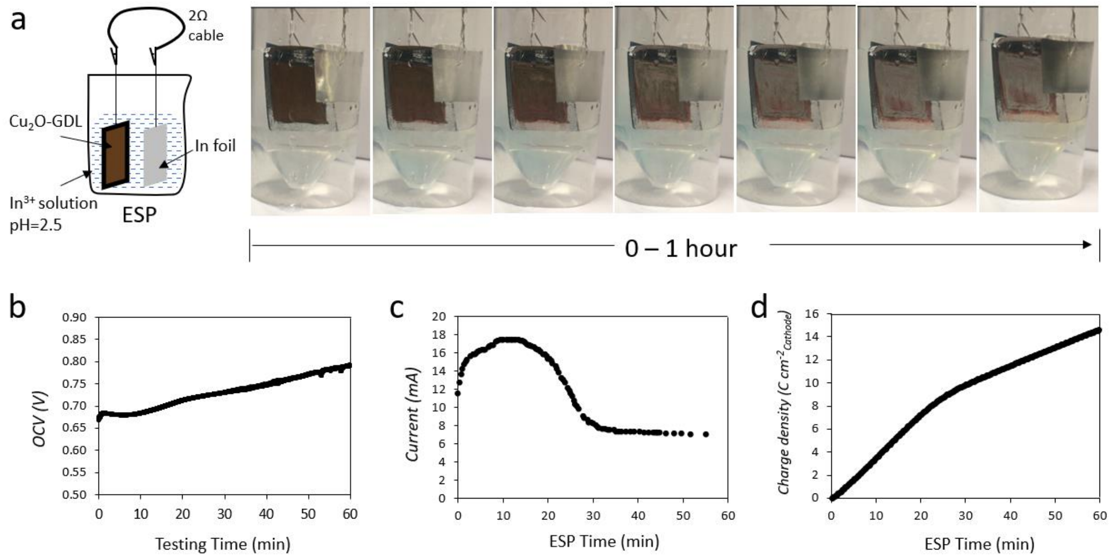

Figure 2. (a) Experiment set-up schematic and process observation for 1 h ESP. (b) Open circuit voltage (OCV) between fresh In foil and Cu_2O-GDL immersed in 0.4 M citric acid mixed 0.05 M $In_2(SO_4)_3$ solution (pH = 2.5), measured for an hour. (c) Current recording during ESP process. (d) The calculated charge density over ESP time.

As indicated in the XRD result in Figure 1a, the Cu_2O-GDL, which got reduced during the ESP process, should be the cathode, so that the In foil should be generating electrons as the anode. Equation (1) – (3) give the anodic and cathodic reactions, and the corresponding half-cell reduction potentials E^0, which were calculated as displayed in Table S1.

$$Anode\ reaction \qquad In \rightarrow In^{3+} + 3e^{-} \tag{1}$$

$E^0 = -0.233$ V vs. SHE, $\Delta G_r^{\ominus} = -67.27$ kJ mol^{-1}

Cathode reaction

$$2CuO + 2e^- + 2H^+ \rightarrow Cu_2O + H_2O \quad (2)$$

$E^0 = +0.668$ V vs. SHE, $\Delta G_r^{\ominus} = -128.83$ kJ mol^{-1}

$$Cu_2O + 2e^- + 2H^+ \rightarrow 2Cu + H_2O \quad (3)$$

$E^0 = +0.463$ V vs. SHE, $\Delta G_r^{\ominus} = -89.30$ kJ mol^{-1}

In precipitation

$$In^{3+} + 3OH^- \xrightarrow{pH \geq 3.4} In(OH)_3 \downarrow \quad (4)$$

The thermodynamic cell potential of (-)In|CuO(+) and (-)In|Cu_2O(+) under reaction conditions in this work is respectively 0.901 and 0.696 V, confirming the measured initial OCV value of 0.68 V to be reasonable. The small amount of CuO in the Cu_2O-GDL should be reduced to Cu_2O firstly as less-negative potential needed in contrast with Cu_2O reduction to Cu. Indium precipitation takes place locally, where pH growth over 3.4[30] by proton consumption caused by Cu oxides reduction, as shown in Equation (4). It is challenging to real-time monitor the local pH variation, however, the growth of bulk pH from 2.5 to 2.8 after 2-hour ESP proved the rise of pH.

As shown in Figure 2a, the colorless solution around the catalyst surface zone turns into light blue, which could be non-electrochemical Cu etching, as demonstrated in Equation (5) and (6).

Cu etching

$$CuO + 2H^+ \rightarrow 2Cu^{2+} + H_2O \quad (5)$$

$$Cu_2O + 2H^+ \rightarrow Cu^{2+} + Cu \downarrow + H_2O \quad (6)$$

The white $In(OH)_3$ layer can be also precipitated on the Cu etching sites where the growth of local pH occurs. This has been verified by another experiment denoted as spontaneous precipitation (SP), which was run at the same condition with ESP but in open circuit without a cable connection as shown in Figure S1. Long-time (2h) SP treatment on Cu_2O-GDL thoroughly etches Cu oxides particles, only $In(OH)_3$ remains on CuIn-SP2h without the existence of Cu species, as indicated by Figure S3 and S5b. This is different from ESP, as CuIn-ESP2h is also a Cu-rich combination with even less $In(OH)_3$ on the surface than CuIn-ESP25min, demonstrated in Figure S4c.

Thus, during the ESP process, there should be two different sites for $In(OH)_3$ precipitation, which commonly increase the local pH - the etching site and reduction site of Cu oxides. Figure 3 illustrates the ESP mechanism. Similar with the SP process at the beginning, the outer layer of Cu oxides is etched by the acidic In^{3+} solution, allowing the initial precipitation of $In(OH)_3$. The electroreduction reaction of the bottomed Cu oxides is carried out simultaneously, which is another site of $In(OH)_3$ precipitation. Cu species still existes with long-time (2h) ESP since the bottomed Cu oxides have been reduced to metallic Cu, which is stable in the acidic solution at the reduction potential. The In coverage unlikely follows up an increasing trend over the ESP time, as measured by XPS survey spectra (Figure S6). The average surface In/Cu atomic ratio of CuIn-ESP15min, CuIn-ESP25min, and CuIn-ESP2h is 0.12, 0.44, and 0.03, respectively, illustrated in Figure 3. It is worth mentioning that this In/Cu ratio should be varied by the depth of XPS detection, the depth here is about 10 nm. In/Cu ratio is increased over the first 25 minutes but decreased afterwards. This is possibly due to the shrunken particles of Cu species during the reduction process, indicated by the SEM image of CuIn-ESP2h in Figure S4b, which are gradually freed from the bond of Nafion binder and collaterally take away the precipitated In species. With more exposed subsurface Cu metal, which unlikely to be the indium precipitation site, the surface In/Cu ratio declines. Linked to the ESP current recording (Figure 2c), the first 15 min with an increasing current should be an accelerating electrochemical process with the reduction of CuO/Cu_2O and Cu_2O/Cu, allowing an increasing amount of $In(OH)_3$ precipitation. However, the non-conductive $In(OH)_3$ layer enhances the resistance of the cathode which may cause the declined ESP current in the next 20 min. After 35 min ESP, the current bottoms out and maintaining around 7.2 mA, which is probably the endpoint of ESP.

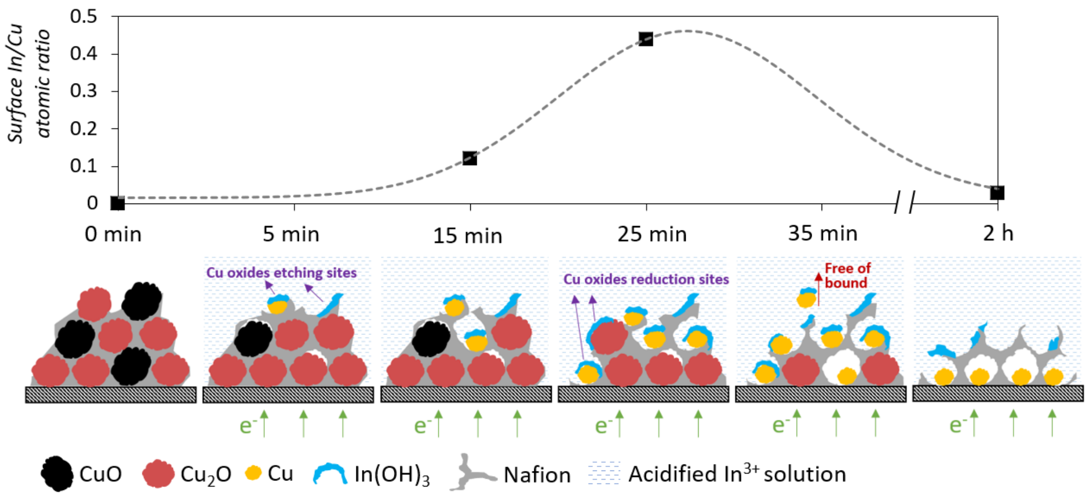

Figure 3. The surface In/Cu atomic ratios and schematic illustration of the electrode surface over ESP time from 0 to 2 hours. Within 5 min: the bottomed CuO and Cu_2O were firstly reduced, with the outmost Cu oxides etching simultaneously. The initial $In(OH)_3$ precipitation site was where the Cu oxides etched. From 5~25 min: with reduction of CuO and Cu_2O ongoing, protons consumed causing local pH increasing, resulting in $In(OH)_3$ precipitation. The surface mass ratio of In/Cu increased during this period as more $In(OH)_3$ precipitated. After 25min: particle size of CuO/Cu_2O shrank after a reduction so that outer Cu particles were gradually freed of the bond of Nafion and collaterally took away the precipitated $In(OH)_3$. With the exposure of the nether Cu without precipitated indium, the surface In/Cu ratio decreased.

2.3. eCO_2R performance using CuIn-ESPs

CuIn-ESP prepared by different precipitation time 5min, 15min, 25min, 35min, and 2h were evaluated by eCO_2R at a wide range of applied potentials (-0.17 ~ -1.17 V vs RHE). The precursor Cu_2O-GDL was also examined denoted as CuIn-ESP0min. A GDE reactor was applied with using 1 M KOH as the catholyte. As previously studied[18], the combination of GDE reactor and alkaline catholyte facilitates CO_2 mass transfer and the overall reaction kinetics. Results of the normalised Faradaic efficiencies (FE) and current density (*j*) are displayed in Figure 4.

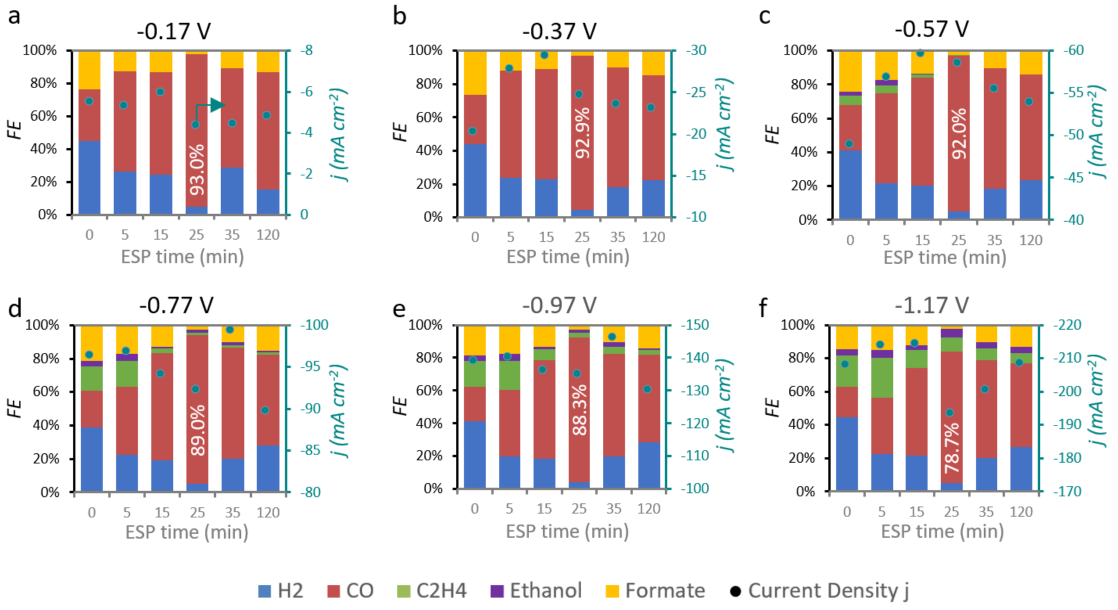

Figure 4. eCO_2R performances of Cu_2O-GDL (ESP 0min) and CuIn-ESP catalysts with different precipitation time at (a) -0.17 V, (b) -0.37 V, (c) -0.57 V, (d) -0.77 V, (e) -0.97 V, (f) -1.17 V (vs. RHE).

At any potential in Figure 4, CuIn-ESP with any precipitation time shows developed CO FE (>50 %) compared to the Cu_2O (ESP 0 min). With the increasing ESP time, CO FE enhances and reaches the maximum value of around 90% with CuIn-ESP25min before decreasing to around 50% with CuIn-ESP2h. On the contrary, FEs of H_2 and formate decrease with the increasing ESP time, reaching their minimal values with CuIn-ESP25min. The difference of product distribution between CuIn-ESP35min and CuIn-ESP2h is small, probably implying the ESP process has been terminated a little while after 35 min, this encounters the preceding assumption. When applying more negative potential, the current density (*j*) and C_2 selectivity increase. The production of C_2 implies the remained catalytic activity of Cu species since Cu is known to be the only metal centre that can form deep reduction products (i.e., $C_{\geq 1}$ hydrocarbons and alcohols)[31-32]. Although the CO FE decreases with more negative potential, the FE sum of CO and C_2 does not change much over the potential: ~93% was maintained in the tested potential range using CuIn-ESP25min. This probably because of the critical intermediate CO*: the CO* dimerization is the rate-determine step of C_2 production[33-37] promoted by high overpotential while the CO* desorption is crucial for CO production which is a potential-independent step[7].

Confirmed by the eCO_2R performance of CuIn-SP2h in Figure S7, $In(OH)_3$ alone is active for formic acid production from eCO_2R, whereas Cu_xO alone (Cu_2O-GDL) is more selective for hydrocarbons under the reaction condition in this study. The contact point of Cu and In species is known for favouring CO formation with suppressed HER[17, 38-39]. This Cu-In interaction was reported to be the Cu-In alloy by Rasul et al.[17], since after introducing indium as a second metal center to Cu, the binding energy of H* was remarkably weakened while CO adsorption energy was substantially unchanged. However, Larrazábal et al.[38] stated the Cu-In alloy was not the main active species for CO evolution since during eCO_2R process the Cu-In composite was evolved with a transition from homogeneous alloy to heterogeneous bimetal, along with the development of CO selectivity. They also found $In(OH)_3$ played a crucial role in favouring the production of CO over Cu–In binary electrocatalysts, which were stably unchanged after eCO_2R. The results from this study confirm their observation and add more insights that the hybrid structure of amorphous $In(OH)_3$ nanolayer capping on polycrystalline Cu_xO facilitates the Cu-In interaction of CO formation from eCO_2R.

From the comparison between CuIn-ESP15min, CuIn-ESP25min, and CuIn-ESP35min, the indium coverage (surface In/Cu ratio) and the phase of copper (either Cu_2O or Cu) that interacted with $In(OH)_3$ are assumed to play key roles in CO selectivity. 0.44 atomic ratio of surface In/Cu (Figure S6b) is considered to be the optimum, which is approximately the maximum achieved during ESP process in this study. Even it is difficult to show either $In(OH)_3/Cu_2O$ or $In(OH)_3/Cu$ is the active site, a higher possibility comes to $In(OH)_3/Cu_2O$ since oxide-derived metal catalyst applied in eCO_2R has been known for reducing the energy barrier of CO_2 activation through strengthening the chemisorption energy of CO_2^-(ads) on reaction sites[2]. Especially for oxide-derived Cu, the subsurface oxygen from the crystal lattice of Cu oxides can enhance the adsorption and rise the coverage of CO*[40-41]. Also, this oxide-derived feature can be maintained during eCO_2R by the "protection" of OH groups from alkaline electrolyte[18, 42].

2.4. Production of CO and tuneable Syngas

Table S2 presents the production rates of all the gas and liquid products from eCO_2R catalysed by Cu_2O-GDL and CuIn-ESPs with different precipitation time, which shows high production rate is enabled by high FE and current density. CuIn-ESP25min with the highest CO selectivity presents high CO yield and CO_2 conversion rate, which are steadily enhancing with the overpotential as displayed in Figure 5a, showing controllable CO production by the energy input. With the highest energy input of -1.17 V, CO_2 conversion and CO yield reach the maximum value at 18.2% and 3.05 mg min^{-1} respectively, with CO_2 supplying at 15 ml min^{-1} on 2 cm^2 working electrode (WE). The potential-dependent CO yield of this work is compared with some related studies[11, 16, 38, 43-46] in Figure 5b, this work shows improvement than the noble Ag-GDE. Interestingly, Syngas could be also produced by CuIn-ESP. Adapting the ESP time or applying different ESP charge density in a more general condition, the CO/H_2 producing ratio is tuneable, as shown in Figure 5c. The CO/H_2 mole ratio was ranging from 1.49 to 14.77 when using CuIn-ESP catalysts with different ESP time from 5 min to 2 h. The stability test of CuIn-ESP25min was carried out at -0.77 V, as shown in Figure S8, the CO FE maintained around 90% for more than 5 hours before suffering the common "flooding" problem in most GDE-based studies[47].

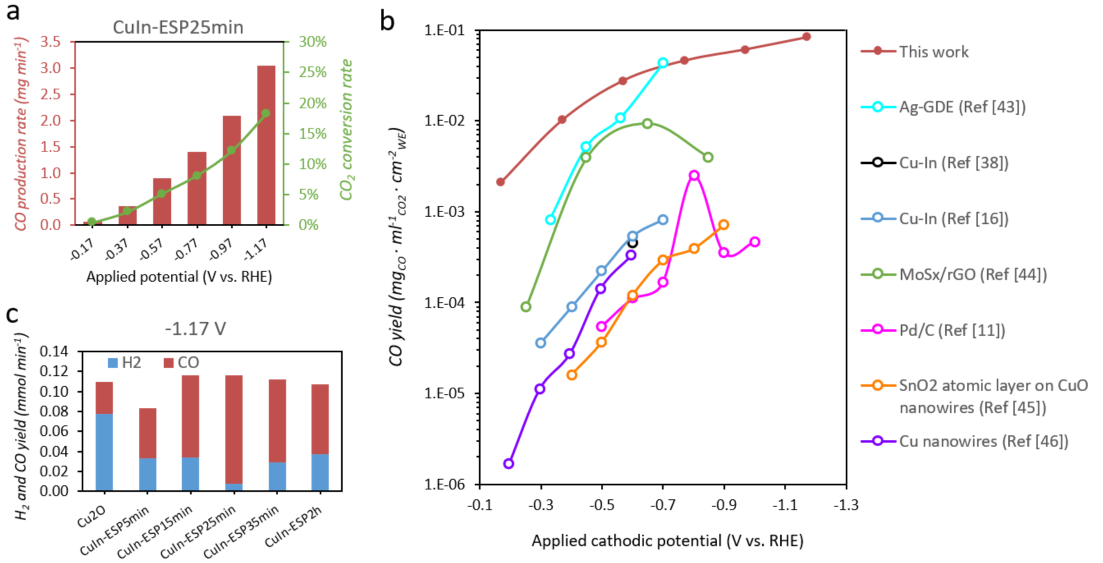

Figure 5. a) CO yield and CO_2 conversion of eCO_2R catalysed by CuIn-ESP25min at a wide range of applied potentials. b) A comparison of CO yield from eCO_2R between this work and other published related studies in recent years. c) Syngas production at -1.17 V from eCO_2R catalysed by Cu_2O, CuIn-ESP5min, CuIn-ESP15min, CuIn-ESP25min, CuIn-ESP35min and CuIn-ESP2h.

3. CONCLUSIONS

A facile ESP method was developed to directly synthesize binary Cu-In catalyst on GDE. It shows a hybrid structure that amorphous $In(OH)_3$ nanolayer (3 ~10 nm thickness) tightly capping on the polycrystalline Cu_xO. The proper Cu-In interaction of this heterostructure enabled ~90% FE of CO production from eCO_2R. In/Cu atom ratio around 0.44 is assumed to play a crucial role in the development of CO selectivity. With the synergy of GDE reactor and 1 M KOH catholyte, both high current density ~ 200 mA cm^{-1} at -1.17 V and high CO FE ~ 90% were achieved by using CuIn-ESP25min. This enabled CO_2 conversion rate and CO yield of 18.2 % and 3.05 mg min^{-1} respectively when CO_2 supplied at 15 ml min^{-1} on 2 cm^2 electrodes. This record CO production from eCO_2R showed improvement than literatures using noble metals as the catalyst. Syngas could also be produced with tuneable CO/H_2 ratio by applying different ESP time when preparing Cu-In catalyst. The potential of scaling up from this bench-scale reaction has also prospected. The present study provides a simple method to construct a catalytic interface with dual active centres, which may bring new insights to the development of novel catalysts in energy conversion and storage fields. Further improvement of this system could be focusing on developing GDE stability, such as using the membrane electrode assembly (MEA)[48].

4. EXPERIMENTAL SECTION

4.1. Preparation of Cu-In catalyst on GDE

The Cu-In catalyst coated GDE was prepared by precipitation of indium species on a Cu_2O- GDL. The Cu_2O-GDL was fabricated by painting commercial Cu_2O particles (EPRUI Nanoparticles & Microsphere Co.Ltd) onto the surface of a tailored commercial GDL (H2315 I2 C6, Freudenberg). In particular, 15 mg

Cu_2O was dispersed in 200 µL isopropanol (> 99.8%, VWR chemicals) and 66 µL 5 wt% Nafion suspension (Sigma-Aldrich) to prepare the catalyst ink. The ink was sonicated for 20 min before layer-by-layer hand-painting onto the 2 cm^2 surface of GDL. Drying process (40 - 50 °C, 1 - 3 min) was applied between each layer. Painting and drying were repeated until the desired catalyst loading of 4~5 mg cm^{-2} was achieved.

To deposit indium species on the Cu_2O-GDL, a pure indium foil (25 mm × 12.5 mm, 99.999%, ADVENT Research Materials Ltd.) and the Cu_2O-GDL and were placed face to face with a 1 cm distance in a 20 ml container. An external cable (2 Ω) was connected between Cu_2O-GDL and In foil to facilitate the redox reaction. The electrochemical spontaneous precipitation (ESP) started from injecting the acidified In^{3+} solution (0.05 M $In_2(SO_4)_3$ and 0.4 M citric acid, pH = 2.5) into the container until immersing the two electrodes. The precipitation duration was controlled by discharging the In^{3+} solution. The OCV was individually monitored by the potentiostat (Metrohm Autolab PGSTAT128N). In another current-monitoring experiment, an amperemeter (1.4 Ω internal resistance) was collected between the In foil and Cu_2O-GDL to record the current variation over the ESP time. For comparison, a non-electrochemical spontaneous precipitation (SP) was carried out without connecting the external cable between In foil and Cu_2O-GDL, as illustrated in Figure S1. All the prepared CuIn-GDEs were rinsed by plenty of DI water and dried at 80 °C in an oven (Oven-30S, SciQuip) for 8 hours.

4.2. Catalysts characterisation

X-ray diffraction (XRD) spectrum to evaluate the crystal structure of the catalyst were obtained by a Philips X-ray diffractometer PW 1730 diffractometer equipped with a Cu X-ray tube (Cu–Kα; λ = 0.154 nm) operated at 40 kV and 40 mA. To determine the elemental compositions and valence states of the electrode surface (~10 nm depth), X-ray photoelectron spectroscopy (XPS) was performed on a Kratos Axis Nova XPS spectrometer using a K-Alpha line X-Ray source (225 W) over an area of approximately 300 × 700 microns. Scanning electron microscopy (SEM, Hitachi SU-70) coupled with an energy dispersive X-ray detector (EDX, Bruker Quantax 400) were applied to initially analyze the catalyst morphology. The microstructures were further analyzed by TEM, HRTEM and SAED on a JEOL3000F at 300 kV. HAADF-STEM and XEDS elemental mapping was performed on a JEOL JEOL3000F with Be double-tilt analytical holder. SAED analysis was performed on JEOL-3000F at 300 kV and the camera length was 255.8 mm. All specimens were prepared by dispersing samples into ethanol and then drop-casted onto holy carbon supported Au grids.

4.3. Catalyst evaluation by eCO_2R

A GDE reactor shown in Figure S2a fabricated by 3D printer (Form 2, Formlabs) using the photoreactive resin (Form 2 Clear Resin, Formlabs) was used to perform the mass transfer developed eCO_2R, as illustrated in our previous study[19]. The anode was Platinum plated Titanium mesh with a dimension of 4 cm^2. Ag/AgCl (RE-5B, BASI, 3 M NaCl, 0.197 V vs. SHE) was used as the reference electrode, and a luggin capillary was applied to prevent it from being damaged in alkaline electrolyte as illustrated in Figure S2b. The applied potentials (vs. Ag/AgCl) in the three-electrode system were all converted to the reversible hydrogen electrode (RHE) according to Equation (7). The potentials stated in this study are referred to RHE unless otherwise stated.

$$\mathrm{E\ (vs.\,RHE) = E\ (vs.\,Ag/AgCl) + 0.197\ V + 0.0591 \times pH} \qquad (7)$$

All the electrochemical reactions and measurements were carried out at ambient temperature and pressure using a potentiostat (Metrohm Autolab PGSTAT128N). The flow rate of CO_2 (BOC 99.99%) was controlled at 15 ml min^{-1} by a flow meter (Cole-Parmer TMR1-010462). 1M KOH (Emsure®, 85%) solution and 5 M KOH solution was employed as the catholyte and anolyte respectively, separated by a cation exchange membrane (CEM) (F-950, Fumapem, 50 μm thickness). The anolyte had a higher K^+ concentration than the catholyte for guaranteeing sufficient cation mobility. A peristaltic pump (120U/DM2, Watson Marlow) was used to supply fresh catholyte to maintain the local pH and to remove liquid product for reaction equilibrium. The flow rate was controlled at 0.25 ml min^{-1} under the applied potential -0.17 ~ -0.77 V and at 0.5 ml min^{-1} under the applied potential -0.77 ~ -1.17 V. eCO_2R was carried out by chronoamperometry (CA) recording the current at a particular applied potential for 30 minutes ranging from -0.17 to -1.17 V. The current density (j) was calculated based on the geometric surface area 2 cm^2 of the working electrode.

4.4. Product analysis of eCO₂R

A gas chromatography (Shimazu Tracera GC-2010) equipped with Barrier Discharge Ionization (BID) detector was used to analyze gas products and alcoholic liquid products. The ShinCarbon ST micropacked column 80/100

(Restek) was used to quantitatively analyze permanent gases and light hydrocarbons, while the Zebron ZB-WAXplus capillary column (Phenomenex) was used for alcoholic liquids. An ion chromatography (Eco IC, Metrohm) equipped with the “METROHM 6.1005.200” column was used for quantifying volatile fatty acids (VFA) including formic acid. A customized standard mixed gas (BOC) with the components of H_2 (1.000%), CO (1.000%), CH_4 (0.500%), CO_2 (96.000%), C_2H_4 (0.500%), C_2H_6 (0.500%), and C_3H_6 (0.500%) were used to quantify the gas products by area normalization method. Liquid products were quantified by the external standard method with creating working curves.

4.5. Calculation of Faradaic efficiencies

The absolute FE for each product was calculated based on Faraday’s law (8) [2], where z is the number of electrons transferred for per mole of reactant (e.g., z = 2 for reduction of CO_2 to CO), n is mass of the product from the electrode in moles, F is Faraday's constant (96485 C mol^{-1}), Q represents the total charge passed.

$$FE = \frac{z\,n\,F}{Q} \tag{8}$$

Liquid products were accumulated continuously and collected for 30 min reaction time, the absolute FEs of liquid products represented average values. Differently, the gas products were collected during a short period of time at the very last minutes of 30 min reaction, the absolute FEs of gas products represented instantaneous values. The bulk catalyst (mostly Cu oxides about 10 mg on each GDE) would be reduced at the first few minutes of eCO_2R when current density reached few tens of mA cm^{-2}, thus electrons should be overall used for eCO_2R

and HER afterwards. To present an average product distribution of 30 min reaction and achieve a more comparable dataset, the FE sum was normalized to 100% with fixing the liquid FEs and proportionally adjusting the gas FEs.

ASSOCIATED CONTENT

Supporting Information

The Supporting Information is available free of charge on the ACS Publications website at DOI:

> Figures of material characterization, including SEM, EDX, XRD, and XPS results; additional CO_2 electroreduction performance.

AUTHOR INFORMATION

Corresponding Author

* E-mail: eileen.yu@ncl.ac.uk

Notes

There are no conflicts to declare.

ACKNOWLEDGMENTS

The authors thank EPSRC LifesCO2R project (EP/N009746/1), EPSRC NECEM (EP/R021503/1) and NERC MeteoRR (NE/L014246/1). Hang Xiang thanks the Doctor Training Awards (SAgE DTA, 2015 cohort) from Faculty of Science, Agriculture and Engineering, Newcastle University for supporting PhD study. The authors are grateful to Ms Maggie White for XRD measurement, Dr Isabel Garcia for SEM/EDX analysis, and Dr David Morgan for partial XPS data collection performed at the EPSRC National Facility for XPS ('HarwellXPS'), operated by Cardiff University and UCL, under contract No. PR16195.

REFERENCES

(1) Spinner, N. S.; Vega, J. A.; Mustain, W. E., Recent Progress in the Electrochemical Conversion and Utilization of CO2. *Catal. Sci. Technol.* **2012,** *2* (1), 19-28.

(2) Zhu, D. D.; Liu, J. L.; Qiao, S. Z., Recent Advances in Inorganic Heterogeneous Electrocatalysts for Reduction of Carbon Dioxide. *Adv. Mater.* **2016,** *28* (18), 3423-3452.

(3) Martín, A. J.; Larrazábal, G. O.; Pérez-Ramírez, J., Towards Sustainable Fuels and Chemicals Through the Electrochemical Reduction of CO2: Lessons from Water Electrolysis. *Green Chem.* **2015,** *17* (12), 5114-5130.

(4) Rasul, S.; Pugnant, A.; Yu, E., Electrochemical Reduction of CO2 at Multi-Metallic Interfaces. *ECS Transactions* **2018,** *85* (10), 57-66.

(5) Yang, J.; Ma, W.; Chen, D.; Holmen, A.; Davis, B. H., Fischer–Tropsch Synthesis: A Review of the Effect of CO Conversion on Methane Selectivity. *Appl. Catal., A* **2014,** *470*, 250-260.

(6) Jahangiri, H.; Bennett, J.; Mahjoubi, P.; Wilson, K.; Gu, S., A Review of Advanced Catalyst Development for Fischer–Tropsch Synthesis of Hydrocarbons from Biomass Derived Syn-Gas. *Catal. Sci. Technol.* **2014,** *4* (8), 2210-2229.

(7) Zhu, W.; Zhang, Y.-J.; Zhang, H.; Lv, H.; Li, Q.; Michalsky, R.; Peterson, A. A.; Sun, S., Active and Selective Conversion of CO2 to CO on Ultrathin Au Nanowires. *J. Am. Chem. Soc.* **2014,** *136* (46), 16132-16135.

(8) Hori, Y.; Wakebe, H.; Tsukamoto, T.; Koga, O., Electrocatalytic Process of CO Selectivity in Electrochemical Reduction of CO2 at Metal Electrodes in Aqueous Media. *Electrochim. Acta* **1994,** *39* (11-12), 1833-1839.

(9) Hatsukade, T.; Kuhl, K. P.; Cave, E. R.; Abram, D. N.; Jaramillo, T. F., Insights into the Electrocatalytic Reduction of CO2 on Metallic Silver Surfaces. *Phys. Chem. Chem. Phys.* **2014,** *16* (27), 13814-13819.

(10) Lu, Q.; Rosen, J.; Zhou, Y.; Hutchings, G. S.; Kimmel, Y. C.; Chen, J. G.; Jiao, F., A Selective and Efficient Electrocatalyst for Carbon Dioxide Reduction. *Nat. Commun.* **2014,** *5*, 3242.

(11) Sheng, W.; Kattel, S.; Yao, S.; Yan, B.; Liang, Z.; Hawxhurst, C. J.; Wu, Q.; Chen, J. G., Electrochemical Reduction of CO2 to Synthesis Gas with Controlled CO/H2 Ratios. *Energy Environ. Sci.* **2017,** *10* (5), 1180-1185.

(12) Gao, D.; Zhou, H.; Wang, J.; Miao, S.; Yang, F.; Wang, G.; Wang, J.; Bao, X., Size-Dependent Electrocatalytic Reduction of CO2 over Pd Nanoparticles. *J. Am. Chem. Soc.* **2015,** *137* (13), 4288-4291.

(13) Wu, J.; Yadav, R. M.; Liu, M.; Sharma, P. P.; Tiwary, C. S.; Ma, L.; Zou, X.; Zhou, X.-D.; Yakobson, B. I.; Lou, J., Achieving Highly Efficient, Selective, and Stable CO2 Reduction on Nitrogen-Doped Carbon Nanotubes. *ACS Nano* **2015,** *9* (5), 5364-5371.

(14) Sharma, P. P.; Wu, J.; Yadav, R. M.; Liu, M.; Wright, C. J.; Tiwary, C. S.; Yakobson, B. I.; Lou, J.; Ajayan, P. M.; Zhou, X. D., Nitrogen-Doped Carbon Nanotube Arrays for High-Efficiency Electrochemical Reduction of CO2: On the Understanding of Defects, Defect Density, and Selectivity. *Angew. Chem., Int. Ed.* **2015,** *54* (46), 13701-13705.

(15) Wu, J.; Ma, S.; Sun, J.; Gold, J. I.; Tiwary, C.; Kim, B.; Zhu, L.; Chopra, N.; Odeh, I. N.; Vajtai, R., A Metal-Free Electrocatalyst for Carbon Dioxide Reduction to Multi-Carbon Hydrocarbons and Oxygenates. *Nat. Commun.* **2016,** *7*, 13869.

(16) Rasul, S.; Anjum, D. H.; Jedidi, A.; Minenkov, Y.; Cavallo, L.; Takanabe, K., A Highly Selective Copper–Indium Bimetallic Electrocatalyst for the Electrochemical Reduction of Aqueous CO2 to CO. *Angew. Chem.* **2015,** *127* (7), 2174-2178.

(17) Jedidi, A.; Rasul, S.; Masih, D.; Cavallo, L.; Takanabe, K., Generation of Cu–In Alloy Surfaces from CuInO2 as Selective Catalytic Sites for CO2 Electroreduction. *J. Mater. Chem. A* **2015,** *3* (37), 19085-19092.

(18) Xiang, H.; Rasul, S.; Scott, K.; Portoles, J.; Cumpson, P.; Eileen, H. Y., Enhanced Selectivity of Carbonaceous Products from Electrochemical Reduction of CO2 in Aqueous Media. *J. CO2 Util.* **2019,** *30*, 214-221.

(19) Rasul, S.; Pugnant, A.; Xiang, H.; Fontmorin, J.-M.; Eileen, H. Y., Low Cost and Efficient Alloy Electrocatalysts for CO2 Reduction to Formate. *J. CO2 Util.* **2019,** *32*, 1-10.

(20) Endrődi, B.; Bencsik, G.; Darvas, F.; Jones, R.; Rajeshwar, K.; Janáky, C., Continuous-Flow Electroreduction of Carbon Dioxide. *Prog. Energy Combust. Sci.* **2017,** *62*, 133-154.

(21) Detweiler, Z. M.; White, J. L.; Bernasek, S. L.; Bocarsly, A. B., Anodized Indium Metal Electrodes for Enhanced Carbon Dioxide Reduction in Aqueous Electrolyte. *Langmuir* **2014,** *30* (25), 7593-7600.

(22) Hoch, L. B.; Wood, T. E.; O'Brien, P. G.; Liao, K.; Reyes, L. M.; Mims, C. A.; Ozin, G. A., The Rational Design of a Single‐Component Photocatalyst for Gas‐Phase CO2 Reduction Using Both UV and Visible Light. *Adv. Sci.* **2014,** *1* (1), 1400013.

(23) Ge, Y.; Kan, K.; Yang, Y.; Zhou, L.; Jing, L.; Shen, P.; Li, L.; Shi, K., Highly Mesoporous Hierarchical Nickel and Cobalt Double Hydroxide Composite: Fabrication, Characterization and Ultrafast NOx Gas Sensors at Room Temperature. *J. Mater. Chem. A.* **2014,** *2* (14), 4961-4969.

(24) Liu, P.; Hensen, E. J., Highly Efficient and Robust Au/MgCuCr2O4 Catalyst for Gas-Phase Oxidation of Ethanol to Acetaldehyde. *J. Am. Chem. Soc.* **2013,** *135* (38), 14032-14035.

(25) Karthik, T. V. K.; Olvera, M. d. l. L.; Maldonado, A.; Gómez Pozos, H., CO Gas Sensing Properties of Pure and Cu-Incorporated SnO2 Nanoparticles: A Study of Cu-Induced Modifications. *Sensors* **2016,** *16* (8), 1283.

(26) Deutsch, K. L.; Shanks, B. H., Active Species of Copper Chromite Catalyst in C–O Hydrogenolysis of 5-Methylfurfuryl Alcohol. *J. Catal.* **2012,** *285* (1), 235-241.

(27) Hou, B.; Sohn, M.; Lee, Y.; Zhang, J.; Sohn, J. I.; Kim, H.; Cha, S.; Kim, J. M., Chemically Encoded Self-Organized Quantum Chain Supracrystals with Exceptional Charge and Ion Transport Properties. *Nano Energy* **2019,** *62*, 764-771.

(28) Hou, B.; Jung, S.; Zhang, J.; Hong, Y.; Kim, B.; Sohn, J. I.; Lee, E. K.; Choi, B. L.; Whang, D.; Cha, S., Growth of Quantum Dot Coated Core-Shell Anisotropic Nanowires for Improved Thermal and Electronic Transport. *Applied Physics Letters* **2019,** *114* (24), 243104.

(29) Hou, B.; Parker, D.; Kissling, G. P.; Jones, J. A.; Cherns, D.; Fermin, D. J., Structure and Band Edge Energy of Highly Luminescent CdSe1–xTex Alloyed Quantum Dots. *Journal of Physical Chemistry C* **2013,** *117* (13), 6814-6820.

(30) Busev, A. I., *The Analytical Chemistry of Indium: International Series of Monographs on Analytical Chemistry*. Elsevier: 2013.

(31) Zhang, L.; Zhao, Z. J.; Gong, J., Nanostructured Materials for Heterogeneous Electrocatalytic CO2 Reduction and Their Related Reaction Mechanisms. *Angew. Chem., Int. Ed.* **2017,** *56* (38), 11326-11353.

(32) Vasileff, A.; Xu, C.; Jiao, Y.; Zheng, Y.; Qiao, S.-Z., Surface and Interface Engineering in Copper-Based Bimetallic Materials for Selective CO2 Electroreduction. *Chem* **2018**, *4*, 1809-1831.

(33) Calle ‐ Vallejo, F.; Koper, M., Theoretical Considerations on the Electroreduction of CO to C2 Species on Cu (100) Electrodes. *Angew. Chem.* **2013,** *125* (28), 7423-7426.

(34) Montoya, J. H.; Shi, C.; Chan, K.; Nørskov, J. K., Theoretical Insights into a CO Dimerization Mechanism in CO2 Electroreduction. *The journal of physical chemistry letters* **2015,** *6* (11), 2032-2037.

(35) Nie, X.; Esopi, M. R.; Janik, M. J.; Asthagiri, A., Selectivity of CO2 Reduction on Copper Electrodes: the Role of the Kinetics of Elementary Steps. *Angew. Chem., Int. Ed.* **2013,** *52* (9), 2459-2462.

(36) DeWulf, D. W.; Jin, T.; Bard, A. J., Electrochemical and Surface Studies of Carbon Dioxide Reduction to Methane and Ethylene at Copper Electrodes in Aqueous Solutions. *J. Electrochem. Soc.* **1989,** *136* (6), 1686-1691.

(37) Schouten, K.; Kwon, Y.; Van der Ham, C.; Qin, Z.; Koper, M., A New Mechanism for the Selectivity to C1 and C2 Species in the Electrochemical Reduction of Carbon Dioxide on Copper Electrodes. *Chem. Sci.* **2011,** *2* (10), 1902-1909.

(38) Larrazábal, G. n. O.; Martín, A. J.; Mitchell, S.; Hauert, R.; Pérez-Ramírez, J., Enhanced Reduction of CO2 to CO over Cu–In Electrocatalysts: Catalyst Evolution Is the Key. *ACS Catal.* **2016,** *6* (9), 6265-6274.

(39) Larrazábal, G. O.; Shinagawa, T.; Martín, A. J.; Pérez-Ramírez, J., Microfabricated Electrodes Unravel the Role of Interfaces in Multicomponent Copper-Based CO2 Reduction Catalysts. *Nat. Commun.* **2018,** *9* (1), 1477.

(40) Kim, D.; Lee, S.; Ocon, J. D.; Jeong, B.; Lee, J. K.; Lee, J., Insights into an Autonomously Formed Oxygen-Evacuated Cu2O Electrode for the Selective Production of C2H4 from CO2. *Phys. Chem. Chem. Phys.* **2015,** *17* (2), 824-830.

(41) Liu, C.; Lourenço, M. P.; Hedström, S.; Cavalca, F.; Diaz-Morales, O.; Duarte, H. A.; Nilsson, A.; Pettersson, L. G., Stability and Effects of Subsurface Oxygen in Oxide-Derived Cu Catalyst for CO2 Reduction. *The Journal of Physical Chemistry C* **2017,** *121* (45), 25010-25017.

(42) Lum, Y.; Ager, J. W., Stability of Residual Oxides in Oxide - Derived Copper Catalysts for Electrochemical CO2 Reduction Investigated with 18O Labeling. *Angew. Chem., Int. Ed.* **2018,** *57* (2), 551-554.

(43) Thorson, M. R.; Siil, K. I.; Kenis, P. J., Effect of Cations on the Electrochemical Conversion of CO2 to CO. *J. Electrochem. Soc.* **2013,** *160* (1), F69-F74.

(44) Li, F.; Zhao, S.-F.; Chen, L.; Khan, A.; MacFarlane, D. R.; Zhang, J., Polyethylenimine Promoted Electrocatalytic Reduction of CO2 to CO in Aqueous Medium by Graphene-Supported Amorphous Molybdenum Sulphide. *Energy Environ. Sci.* **2016,** *9* (1), 216-223.

(45) Schreier, M.; Héroguel, F.; Steier, L.; Ahmad, S.; Luterbacher, J. S.; Mayer, M. T.; Luo, J.; Grätzel, M., Solar Conversion of CO2 to CO Using Earth-Abundant Electrocatalysts Prepared by Atomic Layer Modification of CuO. *Nat. Energy* **2017,** *2* (7), 17087.

(46) Raciti, D.; Livi, K. J.; Wang, C., Highly Dense Cu Nanowires for Low-Overpotential CO2 Reduction. *Nano letters* **2015,** *15* (10), 6829-6835.

(47) Leonard, M. E.; Clarke, L. E.; Forner-Cuenca, A.; Brown, S. M.; Brushett, F., Investigating Electrode Flooding in a Flowing Electrolyte, Gas-Fed Carbon Dioxide Electrolyzer. ChemRxiv **2019**.

(48) Weng, L.-C.; Bell, A. T.; Weber, A. Z., Towards Membrane-Electrode Assembly Systems for CO2 Reduction: a Modeling Study. *Energy Environ. Sci.* **2019**, *12*, 1950-1968.

Supporting Information

Copper-indium binary catalyst on gas diffusion electrode for high-performance CO_2 electrochemical reduction with record CO production efficiency

*Hang Xiang[1], Shahid Rasul[1,2], Bo Hou[3], Jose Portoles[1], Peter Cumpson[1], Eileen H. Yu[1] **

[1] School of Engineering, Newcastle University, Newcastle Upon Tyne

[2] Faculty of Engineering and Environment, Northumbria University, Newcastle Upon Tyne

[3] Engineering Department, University of Cambridge, Cambridge

Corresponding Author

*(eileen.yu@ncl.ac.uk)

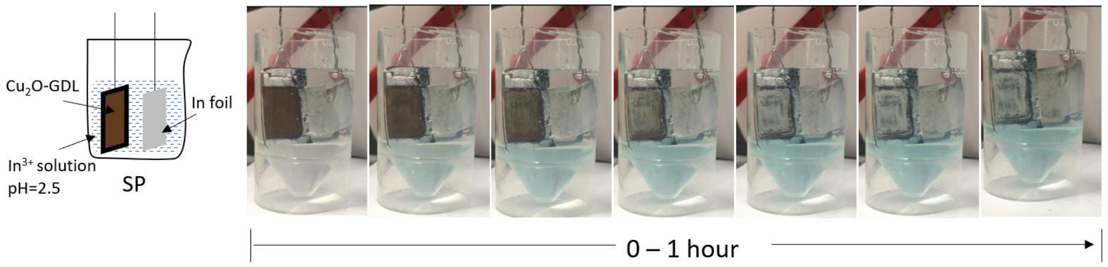

Figure S1. Experiment set-up schematic and process observation for 1 h SP.

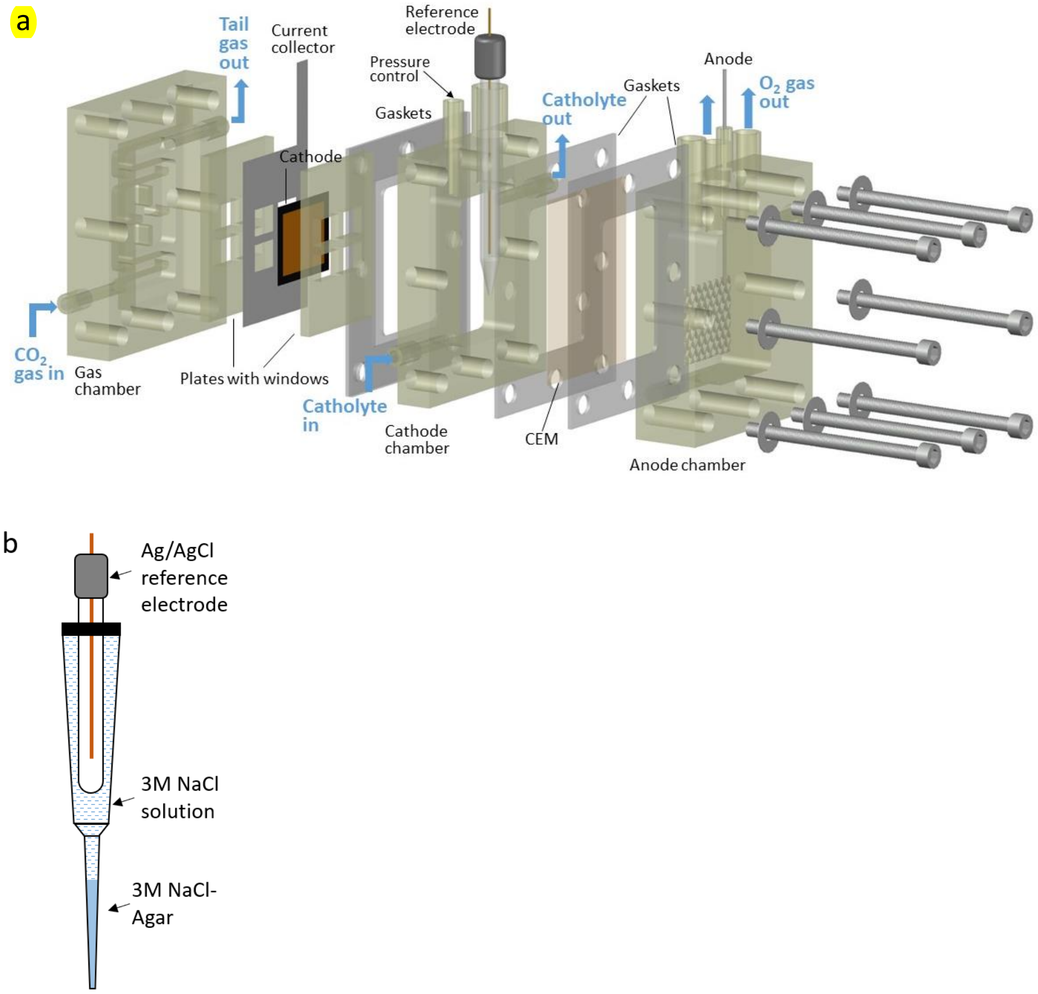

Figure S2. (a) 3D drawing of the GDE reactor set-up used in this study, reprinted from Ref. [1] with permission from the Journal of CO$_2$ Utilization Owner Societies. (b) Schematic of the Ag/AgCl reference electrode with a plastic Lugin capillary.

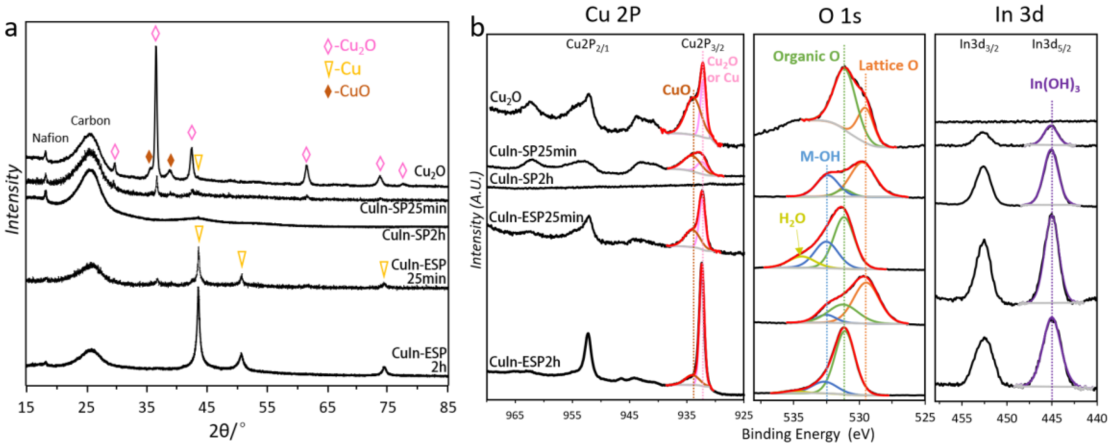

Figure S3. (a) XRD profiles and (b) High-resolution XPS spectrum of Cu 2p, O 1s, and In 3d of Cu_2O-GDL (top), CuIn-SP25min (2nd from top), CuIn-SP2h (3rd from top), CuIn-ESP25min (2nd from bottom), CuIn-ESP2h (bottom).

In Figure S3a, the XRD pattern of Cu_2O confirms Cu_2O is the major phase with a small amount of CuO and Cu. Its $Cu2p_{3/2}$ spectra in XPS analysis (top of Figure S3b) also shows the presence of CuO (933.9 eV) and Cu_2O or Cu (932.3 eV)[2-4]. The O1s spectra can be de-convoluted into two distinct peaks at 529.5 eV and 531.2 eV, attributed to the lattice oxygen from copper oxides and organic oxygen from Nafion binder respectively[5-7].

SP is a Cu vanishing process with substitutional $In(OH)_3$ precipitation, since all the Cu-related peaks attenuated in CuIn-SP25min and disappeared in CuIn-SP2h as presented in Figure S3a. No indium signals can be found on the XRD patterns of either CuIn-SP25min or CuIn-SP2h, however, the XPS spectrum (2nd and 3rd from the top in Figure 3b certificate the existence of indium species on the electrode surface. The prominent photoelectronic peaks in In 3d spectra are symmetrical, at 445.1 eV and 452.5 eV assigned as In $3d_{5/2}$ and In $3d_{3/2}$ of $In(OH)_3$[8,9]. From the XPS O1s spectrum, the M-OH peak can be differentiated at ~532.5 eV in either CuIn-SP25min or CuIn-SP2h, attributed to the formation of $In(OH)_3$[9,10]. The absence of lattice oxygen in the O 1s region as well as the disappearing Cu2p signal of CuIn-SP2h indicate the vanish of Cu species during SP process, in accordance with the XRD results.

ESP is a Cu reduction process with overlapping In(OH)$_3$ precipitation. XRD pattern of CuIn-ESP25min in Figure S3a (2nd from the bottom) rises three strong peaks of metallic Cu with the greatly declined Cu$_2$O peaks. Those metallic Cu peaks get intensified with the absence of Cu oxides in the spectrum of CuIn-ESP2h. This indicates the reduction of Cu oxides during ESP process, and CuIn-ESP with longer precipitation time get higher reduction degree. Indium species is still difficult to be found by XRD, probably implying its amorphous characteristics or an ultrathin surface layer. The XPS results of CuIn-ESP in Figure S3b (1st and 2nd from the bottom) further indicate the reduction of Cu oxides during ESP process. Compared to the Cu2P spectrum of "Cu$_2$O", the CuO peak of CuIn-ESP25min at 933.9 eV in the Cu2p$_{3/2}$ region reduced and Cu$_2$O or Cu (932.3 eV) constituted the major Cu species on the electrode surface. With the ESP prolonged to 2h, the Cu species on the electrode surface might be mostly metallic Cu with the largest Cu$_2$O or Cu peak at 932.3 eV. Even though no In-related signal was found on the XRD, the existence of indium can be observed from the XPS In3d spectra in the form of In(OH)$_3$, same to those of CuIn-SP. The O1s spectra also indicates the reduction of Cu oxides and formation of In(OH)$_3$ during ESP process, since the lattice O peak (529.5 eV) which linked to the crystallized Cu oxides no longer exists in CuIn-ESP2h and the existence of M-OH peak (532.5 eV) which linked to the In(OH)$_3$ in both CuIn-ESP25min and CuIn-ESP2h.

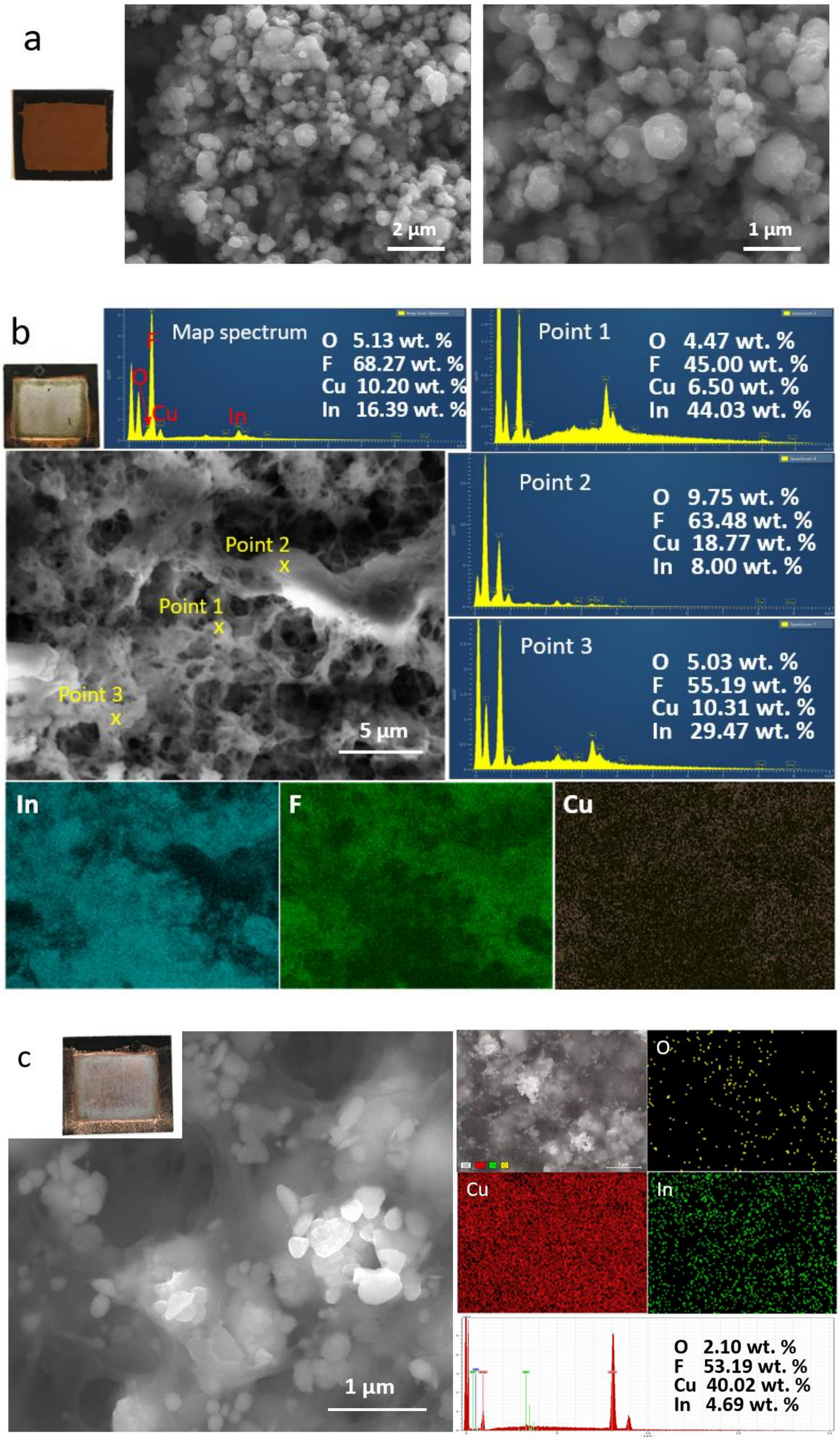

Figure S4. SEM images of (a) Cu_2O-GDL. SEM images, elemental mapping, and quantitative EDX analysis of (b) CuIn-ESP25min and (c) CuIn-ESP2h.

As shown in Figure S4a, the SEM image of fresh Cu_2O presents uniformly distributed polygon particles with the size ranging from 100 to 1000 nm. The surface of CuIn-ESP25min (Figure S4b) presents disordered reticular structure with attaching irregular protrusions in micro-scale. The EDX elemental mapping indicates Cu distributes almost the whole selected area but the distribution areas of In and F are mostly non-overlapping, implying the indium precipitation was majorly taken place on Cu species rather than on Nafion. The EDX result of map spectrum and point scan indicating different kinetics of In precipitation on different sites. The morphology of CuIn-ESP2h in Figure S4c also shows the reticular framework. Different from CuIn-ESP25min, the particles surrounding the framework show more regular crystal structure which are mostly thin triangle prisms (~0.5 mm edge length). The Elemental mapping and EDX results of CuIn-ESP2h indicate those crystalline particles are mostly Cu which embedded in the Nafion framework, with very small amount of In.

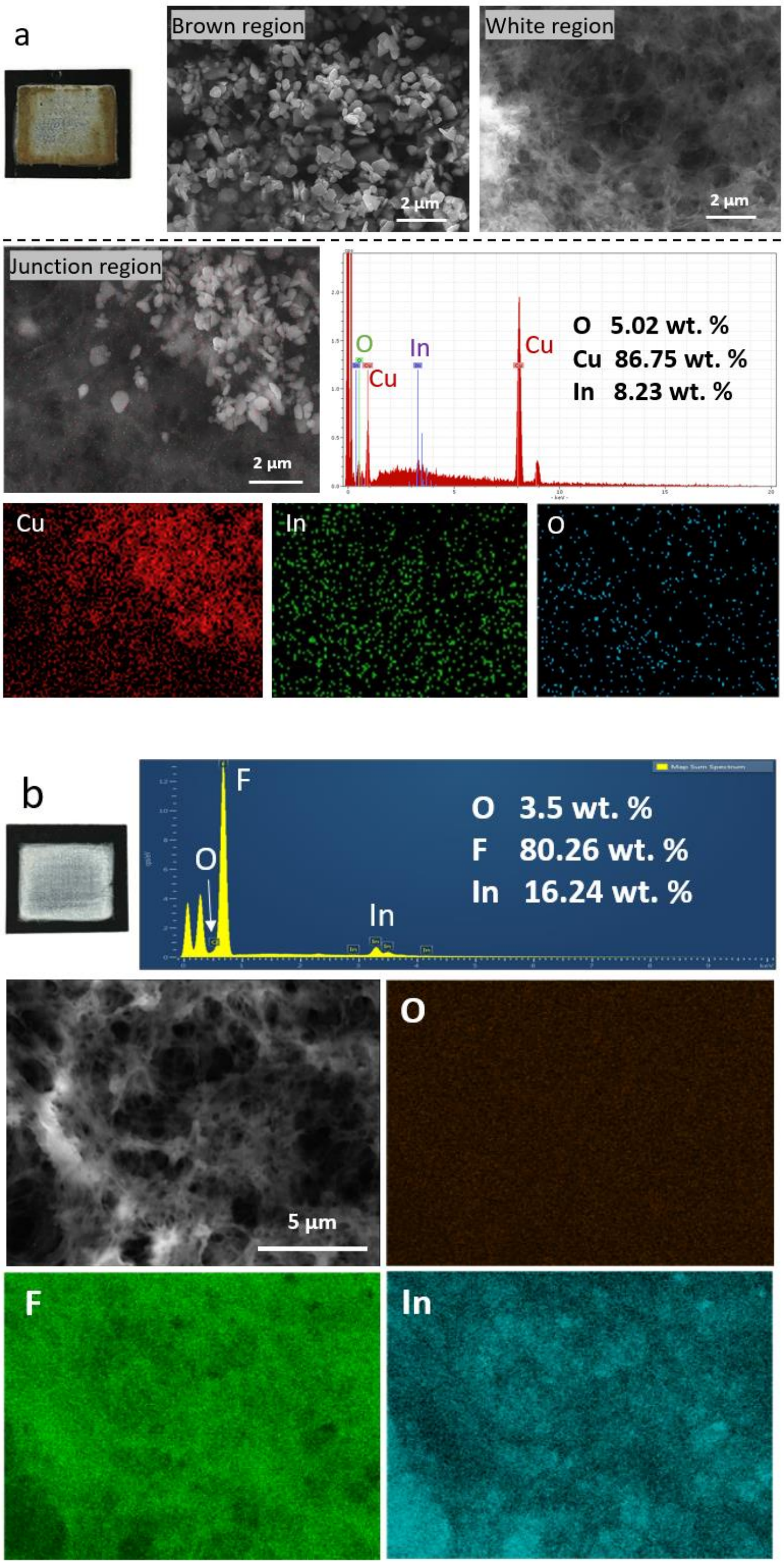

Figure S5. SEM images, elemental mapping, and quantitative EDX analysis of (a) CuIn-SP25min and (b) CuIn-SP2h.

As shown in Figure S5a, the CuIn-SP25min shows obvious brown-white boundary, which in microscale corresponds to the junction of crystalline particles and cloudy reticular structure. The shape of crystalline particles in the brown region is uniformly triangular thin prism with the edge length around 0.5 μm while the reticular material in the white region presents disordered structure. Elemental mapping and EDX were applied to analyse the junction region which confirm the existence of Cu and In and further indicate the triangular prisms are Cu species while In species are mostly distributed on the reticular structure. On the CuIn-SP2h, the crystalline triangular particles completely vanish but the reticular disordered material existed as displayed in Figure S5b. The EDX result also proves the disappearing of Cu species that F and In are the main elements on the surface of CuIn-SP2h, linked to the Nafion binder and indium precipitation layer respectively. The elemental mapping indicates Nafion constitutes the framework of the reticular material while the indium species primarily occupies the pores. The generation of the pores on Nafion framework should be most probably resulted from the disappearing Cu particles where the indium precipitation took place.

(a) CuIn-ESP15min

Average In/Cu atom ratio = 0.12

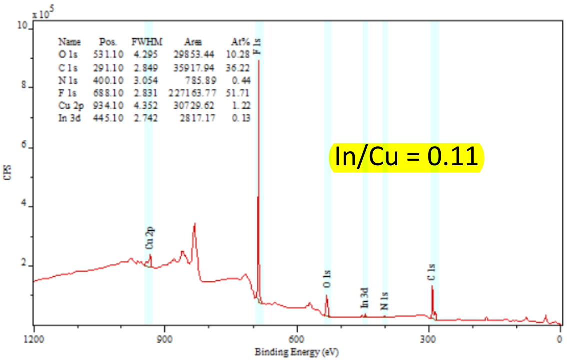

Name	Pos.	FWHM	Area	At%
O 1s	531.10	4.295	29853.44	10.28
C 1s	291.10	2.849	35917.94	36.22
N 1s	400.10	3.054	785.89	0.44
F 1s	688.10	2.831	227163.77	51.71
Cu 2p	934.10	4.352	30729.62	1.22
In 3d	445.10	2.742	2817.17	0.13

In/Cu = 0.11

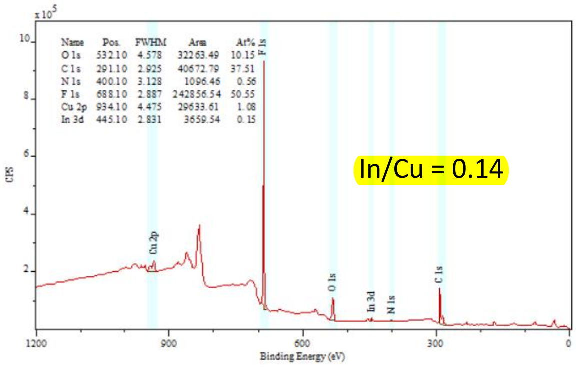

Name	Pos.	FWHM	Area	At%
O 1s	532.10	4.578	32263.49	10.15
C 1s	291.10	2.925	40672.79	37.51
N 1s	400.10	3.128	1096.46	0.56
F 1s	688.10	2.887	242856.54	50.55
Cu 2p	934.10	4.475	29633.61	1.08
In 3d	445.10	2.831	3659.54	0.15

In/Cu = 0.14

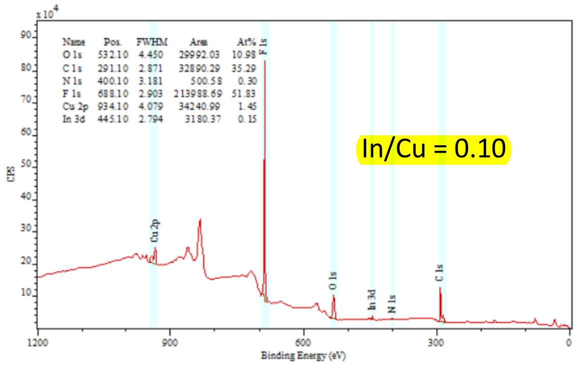

Name	Pos.	FWHM	Area	At%
O 1s	532.10	4.450	29992.03	10.98
C 1s	291.10	2.871	32890.29	35.29
N 1s	400.10	3.181	500.58	0.30
F 1s	688.10	2.903	213988.69	51.83
Cu 2p	934.10	4.079	34240.99	1.45
In 3d	445.10	2.794	3180.37	0.15

In/Cu = 0.10

(b) CuIn-ESP25min

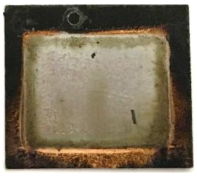

Average In/Cu atom ratio = 0.44

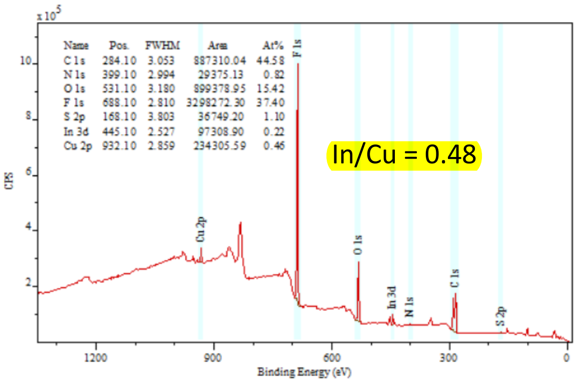

Name	Pos.	FWHM	Area	At%
C 1s	284.10	3.053	887310.04	44.58
N 1s	399.10	2.994	29375.13	0.82
O 1s	531.10	3.180	899378.95	15.42
F 1s	688.10	2.810	3298272.30	37.40
S 2p	168.10	3.803	36749.20	1.10
In 3d	445.10	2.527	97308.90	0.22
Cu 2p	932.10	2.859	234305.59	0.46

In/Cu = 0.48

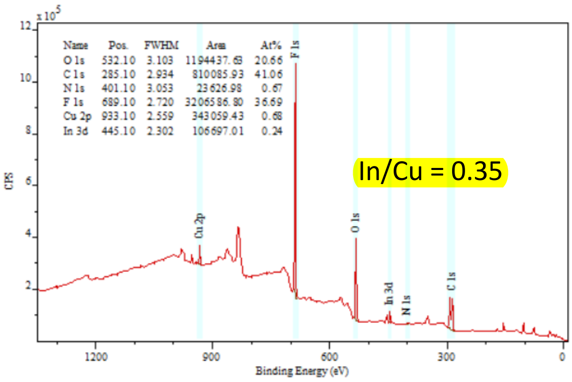

Name	Pos.	FWHM	Area	At%
O 1s	532.10	3.103	1194437.63	20.66
C 1s	285.10	2.934	810085.93	41.06
N 1s	401.10	3.053	23626.98	0.67
F 1s	689.10	2.720	3206586.80	36.69
Cu 2p	933.10	2.559	343059.43	0.68
In 3d	445.10	2.302	106697.01	0.24

In/Cu = 0.35

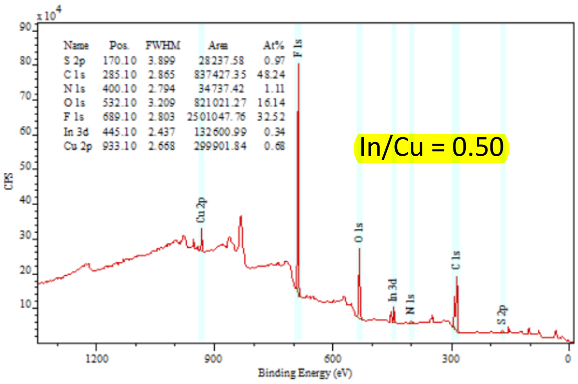

Name	Pos.	FWHM	Area	At%
S 2p	170.10	3.899	28237.58	0.97
C 1s	285.10	2.865	837427.35	48.24
N 1s	400.10	2.794	34737.42	1.11
O 1s	532.10	3.209	821021.27	16.14
F 1s	689.10	2.803	2501047.76	32.52
In 3d	445.10	2.437	132600.99	0.34
Cu 2p	933.10	2.668	299901.84	0.68

In/Cu = 0.50

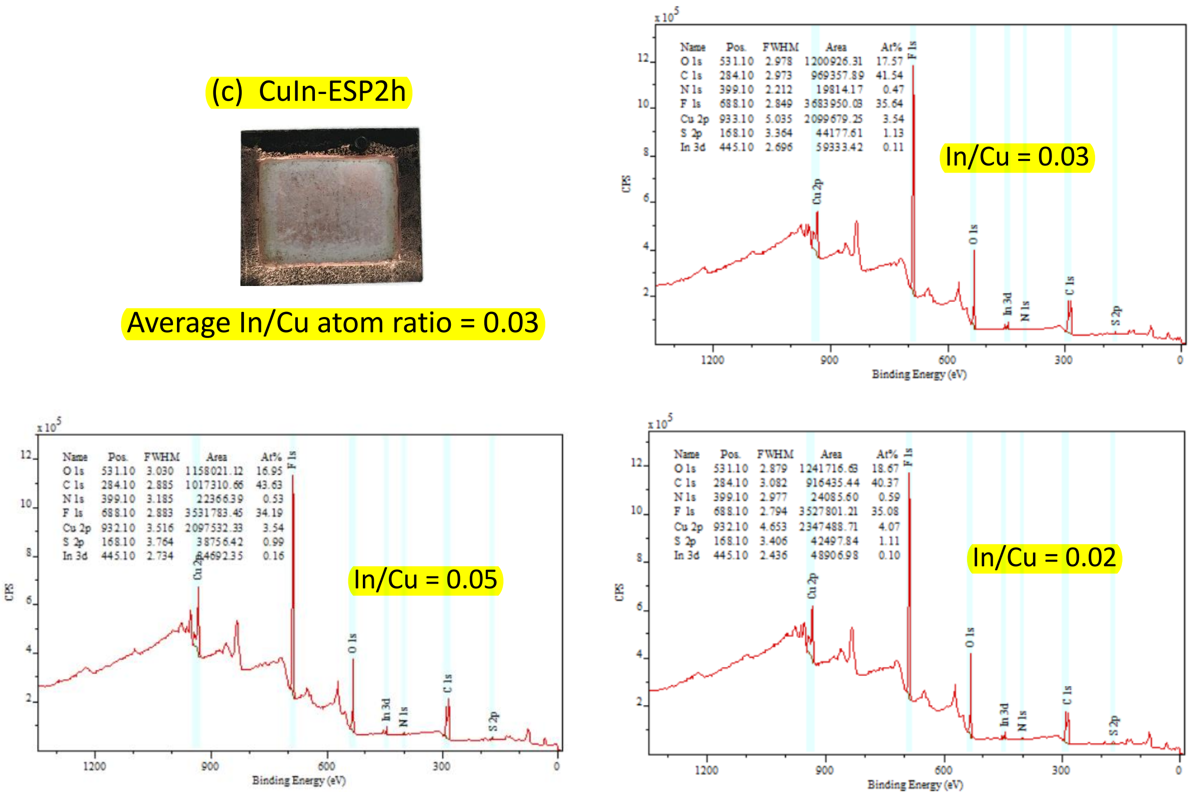

Name	Pos.	FWHM	Area	At%
O 1s	531.10	2.978	1200926.31	17.57
C 1s	284.10	2.973	969357.89	41.54
N 1s	399.10	2.212	19814.17	0.47
F 1s	688.10	2.849	3683950.03	35.64
Cu 2p	933.10	5.035	2099679.25	3.54
S 2p	168.10	3.364	44177.61	1.13
In 3d	445.10	2.696	59333.42	0.11

Name	Pos.	FWHM	Area	At%
O 1s	531.10	3.030	1158021.12	16.95
C 1s	284.10	2.885	1017310.66	43.63
N 1s	399.10	3.185	22366.39	0.53
F 1s	688.10	2.883	3531783.45	34.19
Cu 2p	932.10	3.516	2097532.33	3.54
S 2p	168.10	3.764	38756.42	0.99
In 3d	445.10	2.734	84692.35	0.16

Name	Pos.	FWHM	Area	At%
O 1s	531.10	2.879	1241716.63	18.67
C 1s	284.10	3.082	916435.44	40.37
N 1s	399.10	2.977	24085.60	0.59
F 1s	688.10	2.794	3527801.21	35.08
Cu 2p	932.10	4.653	2347488.71	4.07
S 2p	168.10	3.406	42497.84	1.11
In 3d	445.10	2.436	48906.98	0.10

Figure S6. Multi-point Quantification analysis on XPS survey spectrum of (a) CuIn-ESP15min, (b) CuIn-ESP25min, and (c) CuIn-ESP2h.

Table S1. Calculations on half-cell reduction potentials (in reduction form) involved in ESP process at standard state. Gibbs–Helmholtz equation, Nernst equation were used based on the database from Outokumpu HSC Chemistry 6.0 software.

Half-cell Reactions	$\Delta H_r^{\ominus}$ (KJ)	$\Delta S_r^{\ominus}$ (J K^{-1})	$\Delta G_r^{\ominus}$ (KJ)	E^0 (V vs. SHE)
$In^{3+} + 3e^- \rightarrow In$	104.60	125.2	67.265	-0.233
$2CuO + 2e^- + 2H^+ \rightarrow Cu_2O + H_2O$	-144.83	-53.66	-128.83	0.668
$Cu_2O + 2e^- + 2H^+ \rightarrow 2Cu + H_2O$	-115.23	-86.98	-89.297	0.463

$\Delta G_r^{\ominus} = \Delta H_r^{\ominus} - T\Delta S_r^{\ominus}$ $E^0 = -\frac{\Delta G_r^{\ominus}}{zF}$	$\Delta H_r^{\ominus}$: change in enthalpy at standard state $\Delta S_r^{\ominus}$: change in entropy at standard state $\Delta G_r^{\ominus}$: change in the Gibbs free energy at standard state E^0: standard half-cell reduction potential z: the number of electrons transferred in the half-cell reaction F: Faradaic constant, 96485 C mol^{-1}. T: temperature, here is 298.15 K

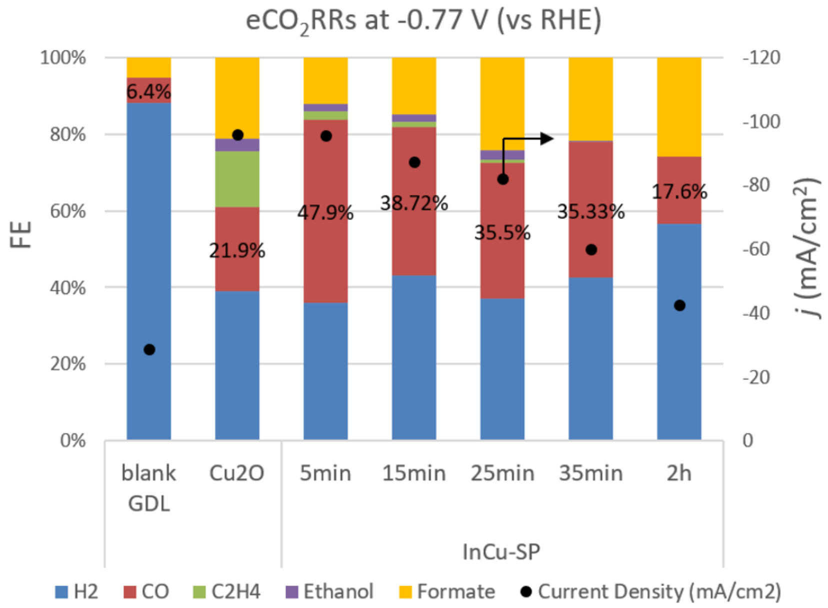

Figure S7. Normalized FE of all the products and current density (*j*) of eCO_2Rs at -0.77 V (vs. RHE) catalysed by blank GDL, Cu_2O-GDL, and CuIn-SP with different precipitation time.

The SP treatment on Cu_2O weakened the capability of C_2 production, only 3.5% C_2 could be produced by CuIn-SP25min and no C_2 produced by CuIn-SP2h. This is in accordance with the vanishing Cu observed by XRD and XPS, as Cu is found to be the only metal centre that can form deep reduction products (i.e., $C_{\geq 1}$ hydrocarbons and alcohols)[11,12]. As the SP time prolonged, CO FE increased to 35.5% by CuIn-SP25min but dropped to 17.6% by CuIn-SP2h. The slight growth of CO production by applying short-time SP implies the evolved interaction between Cu and In, since the Cu-In combination forms the active sites for CO production with suppressed HER[13,14]. However, the formate FE presents a slow-growth trend over the precipitation time, which is an indication of the increasing indium content on the surface as indium is known for the preferential formate production from eCO_2R, either in the form of In metal[8] or $In(OH)_3$[15]. The CuIn-SP2h which contains mainly $In(OH)_3$ without Cu species shows highest formate FE of 25.7%. The current density decreased over the SP time, probably owing to the declined electrode surface area and conductivity during the complete etching of Cu.

Table S2. The practical production amounts of all the gas and liquid products of eCO_2R catalyzed by Cu_2O, CuIn-ESP5min, CuIn-ESP15min, CuIn-ESP25min, CuIn-ESP35min and CuIn-ESP2h.

	Cathode potential (V vs RHE)	**Current density (mA/cm^2)**	**Percentages of gas products in tail gas**				**Yields of liquid products (mg/min)**	
			H_2 %	CO %	C_2H_4 %	CO_2 %	Formate	Ethanol
Cu_2O	-0.17	-5.43	0.19	0.13	0.00	99.68	0.0366	0.000
	-0.37	-20.20	0.70	0.47	0.00	98.84	0.1525	0.000
	-0.57	-48.60	1.91	1.24	0.04	96.80	0.3387	0.005
	-0.77	-96.1	3.58	2.01	0.22	94.19	0.5853	0.015
	-0.97	-139	5.75	2.95	0.36	90.95	0.7446	0.023
	-1.17	-208	11.06	4.58	0.77	83.58	0.8558	0.040
CuIn-ESP5min	-0.17	-5.25	0.10	0.24	0.00	99.66	0.0190	0.000
	-0.37	-27.56	0.65	1.77	0.00	97.58	0.0937	0.000
	-0.57	-56.72	1.26	3.12	0.05	95.58	0.2782	0.009
	-0.77	-96.63	1.86	3.36	0.21	94.56	0.4781	0.019
	-0.97	-140.28	3.14	6.36	0.47	90.03	0.7035	0.029
	-1.17	-213.75	5.12	7.62	0.89	86.36	0.9102	0.051
CuIn-ESP15min	-0.17	-5.92	0.15	0.37	0.00	99.48	0.0221	0.000
	-0.37	-29.23	0.61	1.78	0.00	97.62	0.0922	0.000
	-0.57	-59.40	1.04	3.22	0.02	95.73	0.2338	0.001
	-0.77	-94	1.53	5.10	0.04	93.33	0.3528	0.004
	-0.97	-135.99	2.56	8.25	0.15	89.04	0.5125	0.010
	-1.17	-214.12	5.13	12.50	0.43	81.94	0.7436	0.028
CuIn-ESP25min	-0.17	-4.25	0.02	0.35	0.00	99.64	0.0024	0.000
	-0.37	-24.68	0.10	2.06	0.00	97.85	0.0197	0.000
	-0.57	-58.40	0.27	4.92	0.00	94.81	0.0512	0.000
	-0.77	-92.00	0.43	7.73	0.02	91.82	0.0750	0.007
	-0.97	-134.84	0.53	11.54	0.07	87.86	0.1026	0.013

	-1.17	-193.45	1.14	16.85	0.30	81.70	0.1218	0.049
CuIn-ESP35min	-0.17	-4.40	0.14	0.29	0.00	99.58	0.0132	0.000
	-0.37	-23.48	0.41	1.61	0.00	97.98	0.0665	0.000
	-0.57	-55.23	0.85	3.23	0.00	95.92	0.1655	0.000
	-0.77	-99.175	2.00	6.63	0.02	91.35	0.2848	0.009
	-0.97	-145.7	2.76	8.62	0.10	88.52	0.4427	0.018
	-1.17	-200.125	4.41	12.60	0.27	82.73	0.5946	0.033
CuIn-ESP2h	-0.17	-4.74	0.07	0.30	0.00	99.63	0.0178	0.000
	-0.37	-22.98	0.50	1.43	0.00	98.06	0.0980	0.000
	-0.57	-53.71	1.20	3.16	0.00	95.64	0.2171	0.000
	-0.77	-89.6	2.72	5.27	0.02	91.99	0.3949	0.003
	-0.97	-130.205	3.68	7.00	0.06	89.26	0.5303	0.006
	-1.17	-208.39	5.59	10.61	0.23	83.57	0.7960	0.033

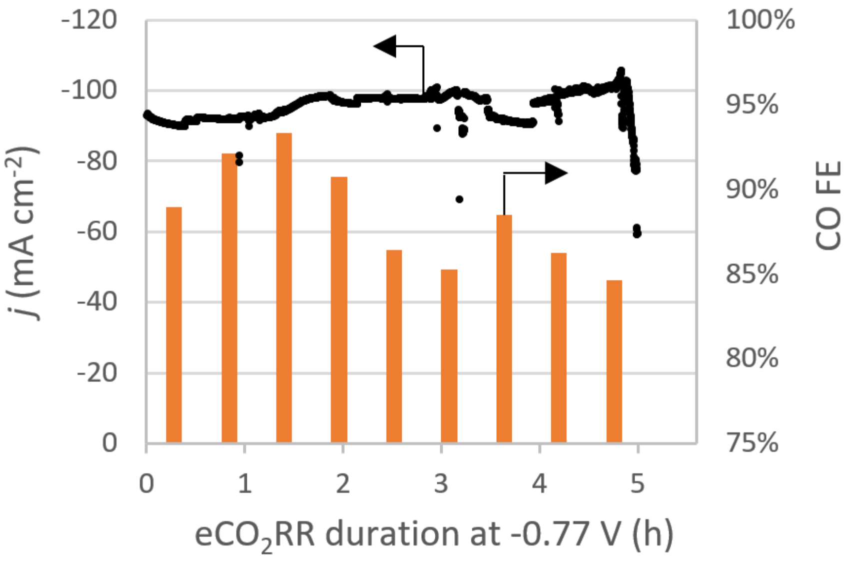

Figure S8. Stability test of CuIn-ESP25min catalysed eCO$_2$R at -0.77 V (vs. RHE)

References

(1) Xiang, H.; Rasul, S.; Scott, K.; Portoles, J.; Cumpson, P.; Eileen, H. Y., Enhanced Selectivity of Carbonaceous Products from Electrochemical Reduction of CO2 in Aqueous Media. *J. CO2 Util.* **2019**, *30*, 214-221.

(2) Liu, P.; Hensen, E. J., Highly Efficient and Robust Au/MgCuCr2O4 Catalyst for Gas-Phase Oxidation of Ethanol to Acetaldehyde. *J. Am. Chem. Soc.* **2013**, *135* (38), 14032-14035.

(3) Karthik, T. V. K.; Olvera, M. d. l. L.; Maldonado, A.; Gómez Pozos, H., CO Gas Sensing Properties of Pure and Cu-Incorporated SnO2 Nanoparticles: A Study of Cu-Induced Modifications. *Sensors* **2016**, *16* (8), 1283.

(4) Deutsch, K. L.; Shanks, B. H., Active Species of Copper Chromite Catalyst in C–O Hydrogenolysis of 5-Methylfurfuryl Alcohol. *J. Catal.* **2012**, *285* (1), 235-241.

(5) Akhavan, O.; Azimirad, R.; Safa, S.; Hasani, E. CuO/Cu(OH)2 Hierarchical Nanostructures as Bactericidal Photocatalysts. *J. Mater. Chem.* **2011**, *21*, 9634-9640.

(6) Liu, P.; Li, Z.; Cai, W.; Fang, M.; Luo, X. Fabrication of Cuprous Oxide Nanoparticles by Laser Ablation in PVP Aqueous Solution. *RSC Adv.* **2011**, *1*, 847-851.

(7) Yu, Y.-H.; Lin, Y.-Y.; Lin, C.-H.; Chan, C.-C.; Huang, Y.-C. High-Performance Polystyrene/Graphene-Based Nanocomposites with Excellent Anti-Corrosion Properties. *Polym. Chem.* **2014**, *5*, 535-550.

(8) Detweiler, Z. M.; White, J. L.; Bernasek, S. L.; Bocarsly, A. B., Anodized Indium Metal Electrodes for Enhanced Carbon Dioxide Reduction in Aqueous Electrolyte. *Langmuir* **2014**, *30* (25), 7593-7600.

(9) Hoch, L. B.; Wood, T. E.; O'Brien, P. G.; Liao, K.; Reyes, L. M.; Mims, C. A.; Ozin, G. A., The Rational Design of a Single-Component Photocatalyst for Gas-Phase CO2 Reduction Using Both UV and Visible Light. *Adv. Sci.* **2014**, *1* (1), 1400013.

(10) Ge, Y.; Kan, K.; Yang, Y.; Zhou, L.; Jing, L.; Shen, P.; Li, L.; Shi, K., Highly Mesoporous Hierarchical Nickel and Cobalt Double Hydroxide Composite: Fabrication, Characterization and Ultrafast NOx Gas Sensors at Room Temperature. *J. Mater. Chem. A.* **2014**, *2* (14), 4961-4969.

(11) Zhang, L.; Zhao, Z. J.; Gong, J., Nanostructured Materials for Heterogeneous

Electrocatalytic CO2 Reduction and Their Related Reaction Mechanisms. *Angew. Chem., Int. Ed.* **2017**, *56* (38), 11326-11353.

(12) Vasileff, A.; Xu, C.; Jiao, Y.; Zheng, Y.; Qiao, S.-Z., Surface and Interface Engineering in Copper-Based Bimetallic Materials for Selective CO2 Electroreduction. *Chem* **2018**, *4*, 1809-1831.

(13) Larrazábal, G. n. O.; Martín, A. J.; Mitchell, S.; Hauert, R.; Pérez-Ramírez, J., Enhanced Reduction of CO2 to CO over Cu–In Electrocatalysts: Catalyst Evolution Is the Key. *ACS Catal.* **2016**, *6* (9), 6265-6274.

(14) Jedidi, A.; Rasul, S.; Masih, D.; Cavallo, L.; Takanabe, K., Generation of Cu–In Alloy Surfaces from CuInO2 as Selective Catalytic Sites for CO2 Electroreduction. *J. Mater. Chem. A* **2015**, *3* (37), 19085-19092.

(15) Rabiee, A.; Nematollahi, D. Electrochemical Reduction of CO2 to Formate Ion Using Nanocubic Mesoporous In (OH)3/Carbon Black System. *Mater. Chem. Phys.* **2017**, *193*, 109-116.